A PSF-Model-based CNN Approach to Enhancing Microscopic Image Resolution

Yu-Ting Cheng[1], Wei-Yun Lee[1] and Liang-Chia Chen[1,#]

1 Department of Mechanical Engineering, National Taiwan University, No. 1, Section 4, Roosevelt Rd., Taipei City, 10617, Taiwan
Corresponding Author / Email: lchen@ntu.edu.tw

KEYWORDS: Image super-resolution, Point spread function, convolutional neural network, precision metrology.

This study addresses the trade-off between high numerical aperture and reduced measurement speed in high-resolution optical systems by proposing a computational method to enhance microscopic image resolution. We present a point spread function (PSF) calibration-based convolutional neural network (CNN) designed to combine the strengths of established super-resolution techniques while mitigating their drawbacks. This model uses a database of measured and parameterized PSFs as its key parameters to improve CNN's interpretability and convergence speed. A custom calibration target measures the system's PSF, mapping its distribution along the axial direction. Through experimental validation, our method effectively boosts the optical resolution of a microscopy system with a numerical aperture of 0.8 to a level of 500 nm, close to the optical diffraction limit.

NOMENCLATURE

CNN = convolutional neural network
PSF = point spread function
RDNN = residual deconvolutional neural network
HR = high-resolution
LR = low-resolution

1. Introduction

Super-resolution [1] is a technique that enhances image quality by reconstructing high-resolution details from low-resolution input. Approaches like deconvolution-based [2] super-resolution and convolutional neural networks [3] are employed to intelligently upscale images, revealing finer features and enabling better visual interpretation. Super-resolution has far-reaching implications for industries requiring precise image analysis and is pivotal in advancing our ability to extract information from images with greater accuracy and fidelity.

1.1. Convolutional neural networks based on super-resolution

Convolutional Neural Networks (CNNs) have emerged as a contemporary technique for enhancing image resolution through the use of deep learning [4,5]. In CNN-based super-resolution, the network is trained on pairs of high-resolution (HR) and low-resolution (LR) images. These models generally come with numerous parameters, enabling them to capture intricate nonlinear relationships within the data. However, this approach is not without drawbacks. One limitation is its dependency on training data [6]. A scarcity of datasets could heighten the risk of model overfitting. Additionally, the complex architecture of CNNs may make it difficult to interpret the rationale behind the weight adjustments during the super-resolution process.

1.2. Deconvolution-based super-resolution

The central concept of deconvolution-based super-resolution hinges on formulating the Point Spread Function (PSF) [7] as a theoretical model [8] and then inverting it to approximate the original image as closely as possible. A precise PSF model allows for the accurate restoration of high-frequency details. However, the challenge lies in accurately modeling the degradation process for real-world situations with complex degradations. Such inaccuracies can result in artifacts like ringing [9].

To address this issue, blind deconvolution methods estimate the PSF by analyzing the blurred input image [10]. However, this approach has limitations. For instance, unpredictable factors like dark currents introduce noise, which is not accounted for in the ideal model. Since the deconvolution process is susceptible to high-frequency noise, this can result in amplified noise in the restored image.

2.Methodology

2.1. PSF modeling

To begin the deconvolution process, it is essential to obtain the PSF of the optical system. Although PSFs can be captured by measuring a

point-like sample, these measurements often suffer from noise or misalignment. To mitigate these effects, we parameterize and fit the measured PSFs. According to Fourier optics [8], the Fourier transform of a PSF with a circular pupil can be assumed circular (see Eq. 1).

$$H(f_x, f_y) = \mathcal{F}(h(x,y))$$
$$H(f_x, f_y) = circ\left(\frac{\sqrt{f_x^2 + f_y^2}}{w/\lambda z}\right) \star circ\left(\frac{\sqrt{f_x^2 + f_y^2}}{w/\lambda z}\right) \quad \text{Eq. 1}$$

According to the Hankel transform, the Fourier transfer of the circular function is the Jinc function [11] (Eq. 2).

$$h(u,v) = ||\omega^2 jinc(\omega\rho)||^2 \quad \text{Eq. 2}$$
$$\omega = \frac{w}{\lambda z} \quad \text{Eq. 3}$$

In Eq. 3, w is the pupil diameter, z is the focus length, and λ is the wavelength. For the aberration, five coefficients are applied from the Seidel coefficients (W), which represent spherical aberration, coma, astigmatism, curvature of field, and distortion (eq. 4).

$$W(\hat{u}_0; \hat{x}, \hat{y}) = W_{040}(\hat{x}^2 + \hat{y}^2)^2 + W_{131}\hat{u}_0(\hat{x}^2 + \hat{y}^2)\hat{x} + W_{222}\hat{u}_0^2\hat{x}^2 + W_{220}\hat{u}_0^2(\hat{x}^2 + \hat{y}^2)\hat{x} + W_{311}\hat{u}_0^3\hat{x} \quad \text{eq. 4}$$

In eq. 4, $\hat{u}_0, \hat{x}, \hat{y}$ are the normalized image height and the exit pupil surface coordinates, respectively. In addition, bias (DC), linear gains (AC), and nonlinear gains (γ) are also considered to increase the flexibility of the model. According to the convolution theorem, the factors mentioned above can be incorporated into the parameterized PSF model, shown in eq. 5.

$$psf(u,v) = \left(DC + AC \left\| \omega(\lambda)^2 jinc(\omega\rho) * \mathcal{F}\left\{se^{jkW(\lambda z f_x, \lambda z f_y)}\right\}\right\|^2\right)^\gamma \quad \text{eq. 5}$$

Earlier models [12] only considered the central wavelength to simplify the calculations. However, a realistic light source encompasses a range of wavelengths. We focus on the wavelength range from 400 nm to 700 nm for more accurate PSF modeling. Weights are then assigned to individual wavelengths based on the intensity spectrum, $(I(\lambda))$, provided in the light source specifications.

The previous model only considers the central wavelength to simplify the model. However, the light source spectrum isn't confined to a single wavelength. For precise PSF modeling, the wavelength range from 400 nm to 700 nm is chosen as the region of interest. Subsequently, weights are assigned to individual wavelengths, guided by the intensity spectrum provided in the light source specifications.

$$psf(u,v) = \sum_{\lambda=n}^{k} I(\lambda)\left(DC + AC\left\|\omega^2 jinc(\omega\rho) * \mathcal{F}\left\{se^{jkW(\lambda z f_x, \lambda z f_y)}\right\}\right\|^2\right)^\gamma \quad \text{eq. 6}$$

In terms of optimization, the Mean Square Error (MSE) [13] is applied as the objective function and utilized by the BADS algorithm [14] for optimization. Once the optimized PSFs are obtained, the deconvolution process can be carried out within the RDNN framework.

2.2. Residual deconvolutional neural network

We introduce the Residual Deconvolutional Neural Network (RDNN), which synergizes CNN-based and deconvolution-based super-resolution techniques. The RDNN initiates with a deconvolution block where both Point Spread Functions (PSFs) and the input image are processed using Wiener-based deconvolution [15]. This is followed by several residual blocks to augment feature extraction capabilities. Finally, three convolution layers act as a decoder to fine-tune detail generation. For loss optimization, we employ the Huber loss function[16], ideal for handling noisy or outlier data, offering a compromise between the sensitivity of Mean Square Error (MSE) and the robustness of Mean Absolute Error (MAE).

In training, our dataset is a hybrid of CAD and deconvolution datasets. The CAD dataset offers high-resolution (HR) synthetic images that are blurred to generate low-resolution (LR) counterparts using PSFs. Conversely, the deconvolution dataset uses microscope-acquired images as LR data, with HR versions created through Wiener-based deconvolution. This diversified dataset enriches the model's capacity for reconstructing intricate details.

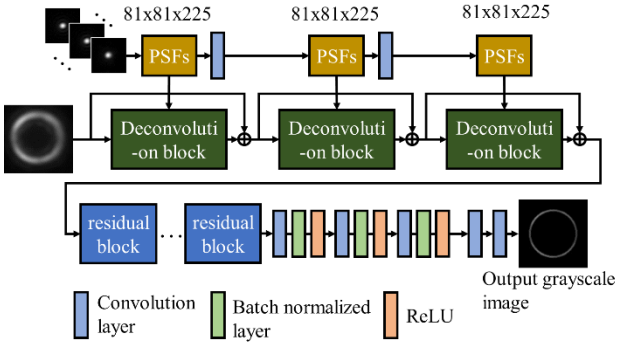

Fig. 1 Architecture of the proposed RDNN.

3. Experimental results and analyses

3.1. System setup for experiments

Table 1 lists the components of the optical system for the experiment. Fig. 2 is the image of the darkfield microscope [17].

Table 1 the components used in the optical system.

light source	Olympus BX3M-PSLED
illumination module	Olympus BXSM-RLA-DF
reflective illumination	Olympus BX3M-LEDR
50x dark field objective lens	Olympus MPLFLN-BD-50x, N.A.0.8
1x tube lens	Olympus U-TLU
CCD	iDS U3-3890CP Rev.2.2

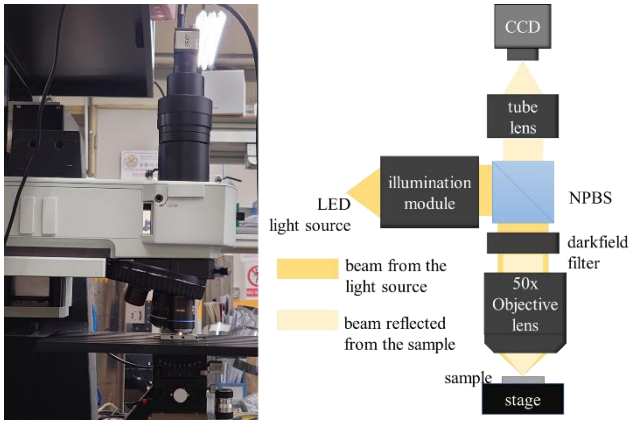

Fig. 2 The image of the darkfield microscope (left), and the schematic of the darkfield microscope (right).

3.2. Methodology of the PSF calibration

The PSFs of the system are obtained through two approaches: measurement and fitting. For the measured PSF, the micro points on the sample are chosen as the reference. The points are small enough to be a point for the experimental system. The darkfield image of the crack is acquired, and the neighbor 81x81 region is taken as the measured PSF. Previous research utilized rough surfaces to acquire multiple spots within a single image to construct a PSF library. However, this approach may introduce potential measurement uncertainties in PSF calibration, resulting in unevenly distributed points across the field of view. To avoid this, by methodically shifting this spot across the focal plane, we capture 225 PSFs within the paraxial region of the darkfield microscope's field of view (see Fig. 3).

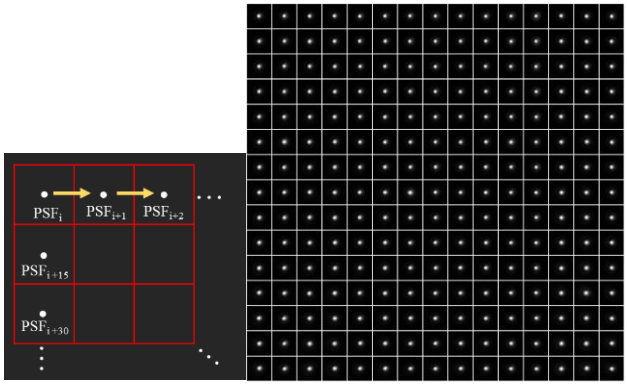

Fig. 3 Schematic for the PSF calibration approach: each time the spot is shifted to a predetermined location, a corresponding PSF is then captured, and the process is repeated until a dataset consisting of 225 PSFs is compiled.

When parameterizing PSFs, we employ a model based on the Jinc function to fit all measured PSFs. Fig. 4 displays a side-by-side comparison of one such measured PSF and its parameterized fitting result. High-order oscillations, or sidelobes, disappear due to low signal-to-noise ratios during image acquisition. However, the fitting process reconstructs these sidelobes, reducing the likelihood of ringing artifacts during deconvolution.

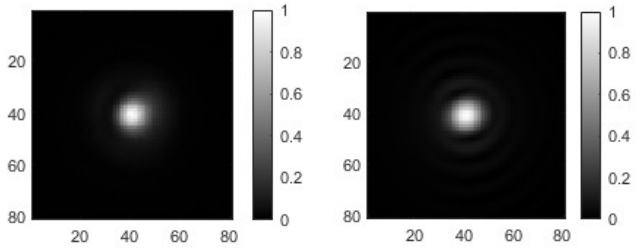

Fig. 4 One of the measured PSF (left) and the corresponding parameterized PSF(right).

3.3. Experimental results and analyses

3.3.1. Experiment with semiconductor micropatterns

Fig. 5 demonstrates the effectiveness of our proposed RDNN method. We use three types of semiconductor micropatterns: a grating, a square block, and a cylinder, all composed of 100 nm height of SiO2 on a Si base. Darkfield images are captured with a microscope at 50x magnification and a numerical aperture of 0.8. Both measured and parameterized PSFs are employed in the Wiener deconvolution process. A library search is conducted to find the most suitable PSFs. Compared to the Wiener method, RDNN visibly suppresses the ringing effect while maintaining image sharpness.

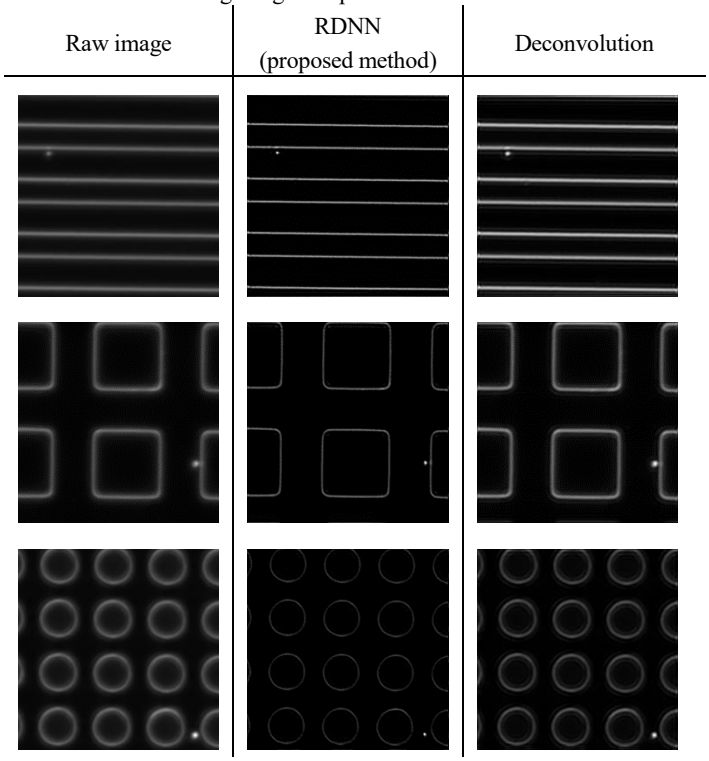

Fig. 5 Comparison between the RDNN and the deconvolution, in which three kinds of structures are shown as grating (top), square block (middle), and cylinder (down).

3.3.2. Experiment with semiconductor micrograting

A micrograting pattern with a nominal linewidth of 500 nm is utilized to validate the optical system's resolution capabilities. The results generated through deconvolution and RDNN methods are depicted in Figure 6, while Figure 7 profiles the contrast of each reconstructed image for comparison. The micrograting structure

becomes more discernible in the deconvolution result than in the raw image, as shown by the yellow line, and even more so in the RDNN output, indicated by the red line. Due to poor signal-to-noise ratios in the raw images, pitch measurement is unfeasible. However, the RDNN-based pitch measurement yields a value of 501.8 ± 34.5 nm, while the deconvolution-based pitch stands at 499.5 ± 47.2 nm. The bias in both methods is less than the digital resolution of 37 nm, with the RDNN's standard deviation even more minor. These results substantiate that the RDNN can more precisely resolve HR structures on a 500 nm lateral-resolution scale than the traditional deconvolution.

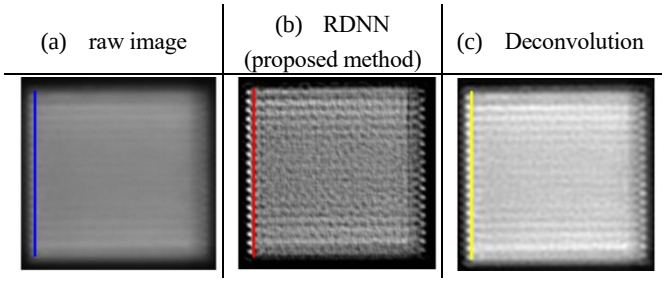

Fig. 6 Reconstructed grating images: (a) raw image acquired from the darkfield microscope, (b) reconstructed image by the proposed RDNN, (c) reconstructed image by the Wiener deconvolution.

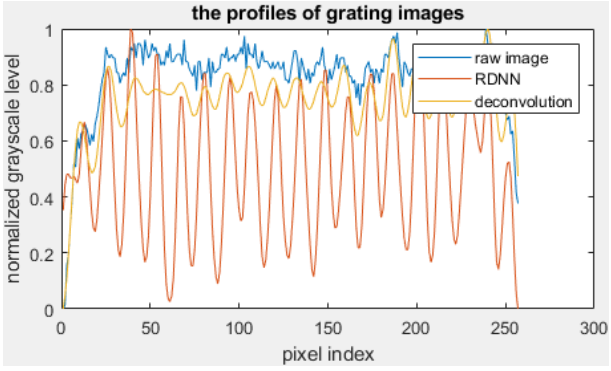

Fig. 7 Image contrast comparison between the raw and different reconstructed images.

4. Conclusions

The Residual Deconvolutional Neural Network (RDNN), a hybrid approach is developed to enhance the optical lateral resolution that integrates Convolutional Neural Networks (CNNs) with optical deconvolution techniques based on Fourier optics. The RDNN enhances image interpretability by incorporating Point Spread Functions (PSFs), acquired via a darkfield microscope. An optical model is employed to fit these PSFs, effectively reducing ringing artifacts. Our findings underscore RDNN'ssuperiority over traditional deconvolution in improving image resolution, particularly in challenging signal-to-noise scenarios. From the initial experimental test results, it is verified that the bias of the linewidth measurement of a semiconductor micrograting pattern is less than 50 nanometers, The method holds significant promise for achieving high-quality image super-resolution.

REFERENCES

1. S. Farsiu, D. Robinson, M. Elad, and P. Milanfar, "Advances and challenges in super-resolution," *International Journal of Imaging Systems and Technology,* vol. 14, no. 2, pp. 47-57, 2004.
2. H. Guo *et al.*, "Elimination of side lobe ghost peak using Wiener deconvolution filter in OFDR," *Journal of Lightwave Technology,* vol. 40, no. 21, pp. 7208-7218, 2022.
3. C. Dong, C. C. Loy, K. He, and X. Tang, "Learning a deep convolutional network for image super-resolution," in *Computer Vision–ECCV 2014: 13th European Conference, Zurich, Switzerland, September 6-12, 2014, Proceedings, Part IV 13*, 2014: Springer, pp. 184-199.
4. X. Chen, X. Wang, J. Zhou, Y. Qiao, and C. Dong, "Activating more pixels in image super-resolution transformer," in *Proceedings of the IEEE/CVF Conference on Computer Vision and Pattern Recognition*, 2023, pp. 22367-22377.
5. B. Lim, S. Son, H. Kim, S. Nah, and K. Mu Lee, "Enhanced deep residual networks for single image super-resolution," in *Proceedings of the IEEE conference on computer vision and pattern recognition workshops*, 2017, pp. 136-144.
6. C. Ledig *et al.*, "Photo-realistic single image super-resolution using a generative adversarial network," in *Proceedings of the IEEE conference on computer vision and pattern recognition*, 2017, pp. 4681-4690.
7. K. Rossmann, "Point spread-function, line spread-function, and modulation transfer function: tools for the study of imaging systems," *Radiology,* vol. 93, no. 2, pp. 257-272, 1969.
8. J. W. Goodman and P. Sutton, "Introduction to Fourier optics," *Quantum and Semiclassical Optics-Journal of the European Optical Society Part B,* vol. 8, no. 5, p. 1095, 1996.
9. A. Mosleh, J. P. Langlois, and P. Green, "Image deconvolution ringing artifact detection and removal via PSF frequency analysis," in *Computer Vision–ECCV 2014: 13th European Conference, Zurich, Switzerland, September 6-12, 2014, Proceedings, Part IV 13*, 2014: Springer, pp. 247-262.
10. E. Faramarzi, D. Rajan, and M. P. Christensen, "Unified blind method for multi-image super-resolution and single/multi-image blur deconvolution," *IEEE Transactions on Image Processing,* vol. 22, no. 6, pp. 2101-2114, 2013.
11. K. A. Wear, A. Shah, and C. Baker, "Spatiotemporal deconvolution of hydrophone response for linear and nonlinear beams—Part II: Experimental validation," *IEEE transactions on ultrasonics, ferroelectrics, and frequency control,* vol. 69, no. 4, pp. 1257-1267, 2022.
12. W.-Y. Lee and L.-C. Chen, "AI-guided optical-model-based super-resolution for semiconductor CD metrology," in *Metrology, Inspection, and Process Control XXXVII*, 2023, vol. 12496: SPIE, pp. 395-403.
13. T. Chai and R. R. Draxler, "Root mean square error (RMSE) or mean absolute error (MAE)?–Arguments against avoiding RMSE in the literature," *Geoscientific model development,* vol. 7, no. 3, pp. 1247-1250, 2014.
14. L. Acerbi and W. J. Ma, "Practical Bayesian optimization for model fitting with Bayesian adaptive direct search," *Advances in neural information processing systems,* vol. 30, 2017.
15. R. Hardie, "A fast image super-resolution algorithm using an adaptive Wiener filter," *IEEE Transactions on Image Processing,* vol. 16, no. 12, pp. 2953-2964, 2007.
16. G. P. Meyer, "An alternative probabilistic interpretation of the huber loss," in *Proceedings of the ieee/cvf conference on computer vision and pattern recognition*, 2021, pp. 5261-5269.
17. H. Ueno *et al.*, "Simple dark-field microscopy with nanometer spatial precision and microsecond temporal resolution," *Biophysical journal,* vol. 98, no. 9, pp. 2014-2023, 2010.